ACS APPLIED MATERIALS & INTERFACES

Research Article

www.acsami.org

# Folic Acid-Conjugated MnO Nanoparticles as a $T_1$ Contrast Agent for Magnetic Resonance Imaging of Tiny Brain Gliomas

Ning Chen,[†] Chen Shao,[‡] Yanming Qu,[†] Shuai Li,[‡] Wei Gu,*[,‡] Tingting Zheng,[‡] Ling Ye,*[,‡] and Chunjiang Yu*[,†]

[†]Department of Neurosurgery, Beijing Sanbo Brain Hospital, Capital Medical University, Beijing 100093, P. R. China

[‡]School of Chemical Biology and Pharmaceutical Sciences, Capital Medical University, Beijing 100069, P. R. China

**ABSTRACT:** Detection of brain gliomas at the earliest stage is of great importance to improve outcomes, but it remains a most challenging task. In this study, oleic acid capped manganese oxide (MnO) nanoparticles (NPs) were prepared by the thermal decomposition of manganese oleate precursors and then transformed to water-dispersible MnO NPs by replacing oleic acid with *N*-(trimethoxysilylpropyl) ethylene diamine triacetic acid (TETT) silane. The covalently bonded TETT silane offers MnO NPs colloidal stability and abundant carboxylic functional groups allowing the further conjugation of the glioma-specific moiety, folic acid (FA). Moreover, the thin layer of TETT silane ensures a short distance between external Mn ion and water proton, which endows the FA-conjugated, TETT modified MnO (MnO-TETT-FA) NPs a longitudinal relaxivity as high as 4.83 $mM^{-1}$ $s^{-1}$. Accordingly, the in vivo magnetic resonance (MR) images demonstrated that MnO-TETT-FA NPs could efficiently enhance the MRI contrast for tiny brain gliomas. More importantly, due to the specificity of FA, MnO-TETT-FA NPs led to a clearer margin of the tiny glioma. This together with the good biocompatibility discloses the great potential of MnO-TETT-FA NPs as effective MRI contrast agents for the early diagnosis of brain gliomas.

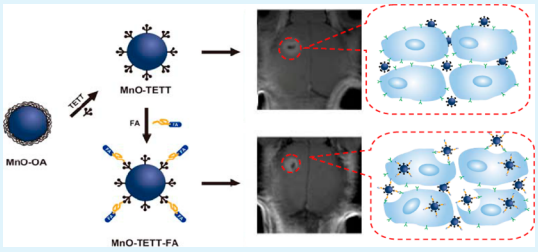


**KEYWORDS:** *manganese oxide nanoparticles (MnO NPs), tiny brain glioma, magnetic resonance imaging (MRI), folic acid (FA)*

## 1. INTRODUCTION

Malignant gliomas are the most common and deadly primary brain tumor with a high recurrence rate and mortality rate within 2 years of diagnosis. The accurate detection and precise delineation of gliomas at the earliest stage are of great importance to improve outcomes. Magnetic resonance imaging (MRI) is the prevailing method for the diagnosis of gliomas preoperatively, and contrast agents are commonly used to further enhance the contrast.[1,2] Currently, Gd-chelates are the mainly used $T_1$ contrast agents for the diagnosis of brain tumors.[3,4] Nonetheless, the nonspecific biodistribution and rapid elimination of Gd-chelates significantly deteriorate their efficacy in accurate diagnoses.[5,6] To address this, nanoparticle-based $T_1$ contrast agents that could passively accumulate in the tumor have been explored as promising alternatives for the MRI of brain tumors.[7,8]

In the past few years, increasing attention has been paid to Mn-based nanoparticles (NPs) due to better performance in detection of brain diseases. Shin et al. prepared manganese oxide (MnO) NPs with a relaxivity of 1.42 $mM^{-1}$ $s^{-1}$ and demonstrated their MRI contrast efficiency in a mouse brain upon local injection with MnO NPs.[9] Chen's group reported that human serum albumin modified MnO NPs with a relaxivity of 1.97 $mM^{-1}$ $s^{-1}$ could induce a prominent $T_1$ contrast in the U87MG glioblastoma xenograft model.[10] Unfortunately, the relaxivities of most reported MnO NPs[11−14] were less than that of Gd-based contrast agents.[15] This means that a larger dose of contrast agents should be administrated to satisfy the contrast enhancement requirement. Meanwhile, although MnO NPs tend to passively accumulate in brain tumors due to the enhanced permeability and retention (EPR) effect, this passive targeting has limitations because of its random delivery mode.[16] In addition, MnO NPs may encounter the problem of diffusion from the tumor site due to their inability to adhere or penetrate into glioma cells, which inevitably leads to an obscure tumor margin.[17] Therefore, glioma-specific MnO NPs with an improved $r_1$ relaxivity are highly desirable for the accurate diagnosis and delineation of gliomas, especially for the tiny ones. Moreover, the specific targeting makes MnO NPs a safer contrast agent by reducing the dosage and minimizing the damage to normal tissues.

Specific contrast agents are generally fabricated by the conjugation of tumor-specific recognition targeting moieties.[18] Antibodies are thought of as one of the most efficient glioma-specific targeting moieties. However, an increased immunogenicity and a limited tissue penetration possibly restrict their in vivo applications.[19,20] Alternatively, small molecule folic acid (FA), which shows a high affinity toward a folate receptor that is not only overexpressed in brain cancer but also expressed at the brain−blood barrier, has been utilized as an effective targeting molecule toward glioma.[21−24] Recently, FA conjugated iron oxide NPs as tumor-specific MRI contrast agents

**Received:** August 5, 2014
**Accepted:** October 21, 2014
**Published:** October 21, 2014

 © 2014 American Chemical Society 

have been demonstrated.[21,25,26] Nevertheless, such $T_2$ contrast agents usually suffer from the drawbacks of the negative contrast effect and magnetic susceptibility artifacts.[15,27] In contrast, development FA conjugated MnO NPs as glioma-specific $T_1$ contrast agents for MRI of tiny gliomas remains unexplored.

Apart from specificity, the colloidal stability of MnO NPs is another critical issue that should be addressed prior to in vivo MRI. Typically, MnO NPs are fabricated by thermal decomposition of metal precursors in organic media. Ligands such as serum albumin,[10] polyethylene glycol(PEG)-phospholipid,[28] and dimercaptosuccinic acid[29] have been used to replace oleoic acid and convert MnO NPs into hydrophilic ones. However, the above-mentioned ligands were bound to MnO NPs by a noncovalent mode, which might not be strong enough to ensure their long-term stability in vivo. In our previous work, the *N*-(trimethoxysilylpropyl) ethylene diamine triacetic acid (TETT) silane, which could covalently attach to the surface of MnO NPs and contains three carboxylic groups per molecular, was employed not only to render NPs with highly colloidal stability but also provide functional groups for further surface manipulation.[30] More importantly, compared to a mesoporous silica coating,[14] the molecular thickness of silane layer shortens the distance between external Mn ion and water proton and an improved $r_1$ relaxivity is thereby expected.[31,32]

Herein, oleic acid capped MnO (MnO-OA) NPs were first prepared by the thermal decomposition method to ensure the uniform size and high crystallinity. Then, highly water-dispersible MnO-TETT NPs were yielded by exchanging oleic acid with TETT silane. Finally, FA was conjugated onto MnO-TETT to produce MnO-TETT-FA NPs that are capable of specificly targeting glioma cells (Scheme 1). The potential of

**Scheme 1. Synthesis of MnO-TETT-FA NPs as Glioma-Specific MRI Contrast Agents**

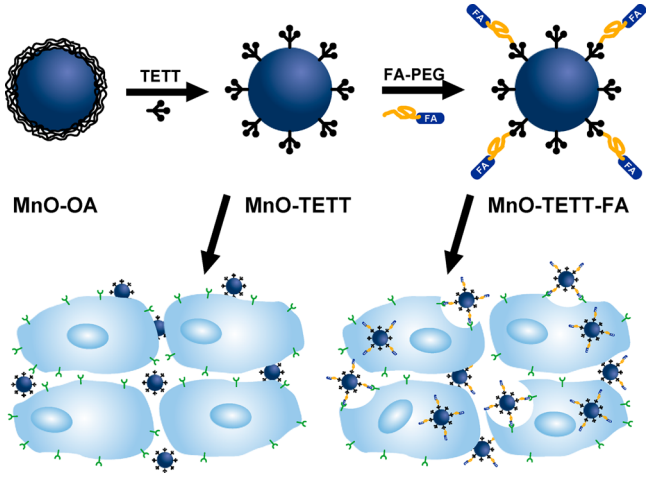


MnO-TETT-FA NPs as glioma-specific $T_1$ contrast agents for MRI and delineation of tiny brain gliomas was disclosed. In addition, the biocompatibility of MnO-TETT-FA NPs was proved in vitro and in vivo.

## 2. EXPERIMENTAL SECTION

**Materials.** Manganese chloride tetrahydrate, sodium oleate, and folic acid-polyethylene glycol (FA-PEG) were purchased from Sinopharm Chemical Reagent (Beijing, China). *N*-(trimethoxysilyl-propyl) ethylene diamine triacetic acid (TETT) silane (45% in water) was supplied by Gelest, Inc. *N*-Hydroxysuccinimide (NHS) and 3-(3-(dimethylamino)propyl)-1-ethylcarbodiimide (EDC) were purchased from Acros Oganics (Geel, Belgium). Fetal bovine serum (FBS) and Dulbecco's modified Eagle's medium (DMEM) were obtained from Gibco (Basel, Switzerland). Methyl thiazolyl tetrazolium (MTT) cell proliferation assay kit was obtained from Amresco. All other chemicals and reagents were of analytical grade and used as received.

**Preparation of Mn-oleate.** To a mixture composed of 40 mL of ethanol, 30 mL of distilled water, and 70 mL of *n*-hexane, 3.96 g of manganese chloride tetrahydrate, and 12.17 g of sodium oleate were added. The mixture was heated to 70 °C and maintained at this temperature for 4 h. The resulting solution was then transferred to a separatory funnel, and the upper organic layer containing the Mn-oleate complex was washed three times with distilled water. The evaporation of the hexane solvent produced the pink colored Mn-oleate powder.

**Preparation of Oleic Acid Coated MnO (MnO-OA) NPs.** The preparation of oleic acid capped MnO NPs was followed the procedure describe elsewhere with minor modifications.[28] Briefly, 2.468 g of the Mn-oleate precursor was dissolved in 50 mL of 1-octadecene. The mixture was degassed at 100 °C for 15 min under vacuum to remove the water and oxygen and, then, was heated to 310 °C and maintained at this temperature for 10 min with $N_2$ purging. After being cooled to room temperature, 200 mL of ethanol was added and the waxy precipitate was retrieved by centrifugation (6000 rpm, 10 min). After washing with acetone three times, the purified precipitate was dispersed in *n*-hexane. The suspension was centrifuged and the supernatant was collected and subjected to freeze-drying.

**Exchange of Oleic Acid with TETT Silane.** To render MnO NPs water dispersible and colloidal stability, TETT silane was employed to replace the oleic acid.[30] Typically, 50 mg of MnO-OA NPs were dispersed in anhydrous toluene, followed by addition of 30 $\mu$L of acetic acid. After sonicating for 15 min, 200 $\mu$L of TETT silane was added. The suspension was stirred at 70 °C for 48 h. Then, the precipitates were collected and washed with toluene and methanol three times, respectively. Finally, the MnO-TETT NPs were dispersed in deionized water and dialyzed against deionized water for 24 h using a cellulose membrane bag (MWCO = 8000−12 000 Da). The purified MnO-TETT NPs was obtained by lyophilization.

**Conjugation of FA-PEG onto MnO-TETT NPs.** The FA-PEG was conjugated to MnO-TETT via the formation of amide bond between the carboxyl groups of MnO-TETT and the amino groups of FA-PEG.[33] Briefly, 100 mg of MnO-TETT NPs was dispersed in 20 mL PBS (0.1 mol $L^{-1}$, pH = 6.0) followed by addition of 1.93 mg of NHS and 1.28 mg of EDC. The activated MnO-TETT NPs was then allowed to react with 10 mg FA-PEG at room temperature for 24 h in PBS (pH 8.0). When the reaction was completed, the suspension was dialyzed against deionized water for 24 h and then subjected to freeze-drying.

**Characterization.** Transmission electron microscopy (TEM) images of MnO NPs were obtained on JEM-2100F (JEOL, Japan) at operating voltage of 100 kV. For TEM imaging, samples were prepared by spreading a drop of sample on copper grids, followed by evaporation under vacuum. Magnetic hysteresis loop of MnO-OA NPs was analyzed on a vibrating sample magnetometer at room temperature. The hydrodynamic diameter and zeta potential of MnO NPs were measured on a Nano-ZS90 Zetasizer (Malvern, UK). X-ray diffraction (XRD) was carried out with a Rigaku SmartLab X-ray diffractometer (Cu−K$\alpha$ radiation $\lambda$ = 1.54056 Å) operating at 40 kV and 40 mA. Fourier transform infrared spectra (FTIR) were recorded on a Nicolet Avatar 300 FT-IR spectrometer (Thermo Nicolet Instrument Corp., USA). The UV−vis absorption spectra were recorded on a UV-3010 spectrophotometer (Hitachi, Japan) using a 1 cm path length cuvette. The content of Mn was determined on an inductively coupled plasma optical emission spectrometry (ICP-OES, Varian 710-ES, USA).

**Relaxivity.** To determine the $T_1$ relaxivity, the particles were diluted in distilled water in Mn concentrations in the range of 0−0.05 mM. The $T_1$ relaxation times of the suspensions were determined using a 7.0 T whole-body MR scanner (Bruker Pharmascan,

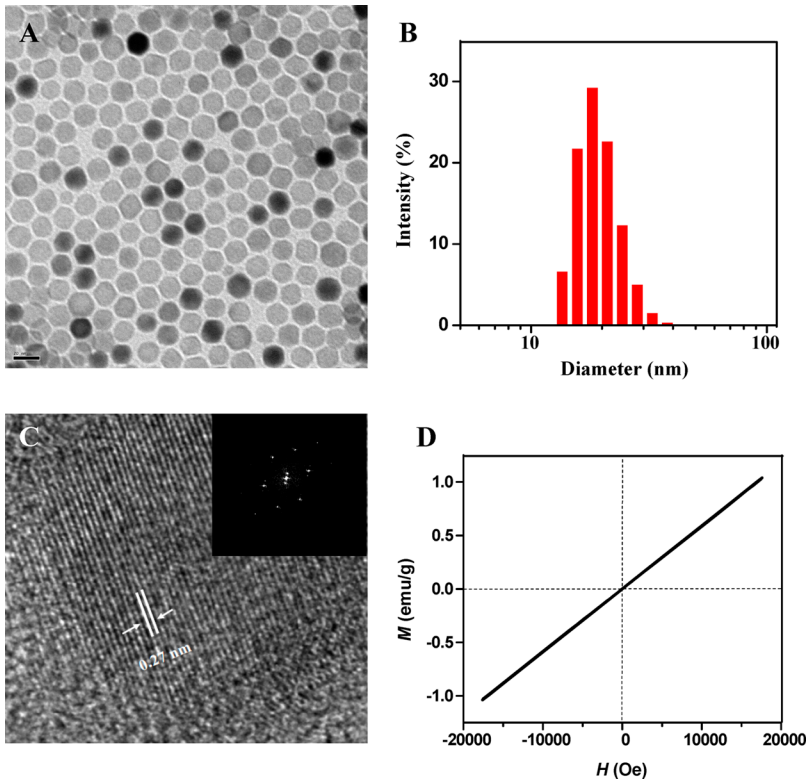


**Figure 1.** TEM image (A) and DLS size distribution (B) of MnO-OA NPs. (C) HRTEM imaging of an individual MnO-OA. (inset) Corresponding SAED pattern and (D) magnetic hysteresis loop of MnO-OA NPs.

Germany). The parameters are following: repetition time (TR) 500.00 ms, multiple echo times (TE) 11.0, 33.00, 55.00, 77.00, and 99.00 ms, field of views (FOV) = 4.0 cm × 4.0 cm, flip angle (FA) = 180.0° and slice thickness = 1 mm. The corresponding relaxation time ($T_1$) of each solution was obtained. Relaxivity values of $r_1$ were calculated through the curve fitting of $1/T_1$ relaxation time ($s^{-1}$) versus the $Mn^{2+}$ concentration (mM).

**MTT Assay.** C6 glioma cells were cultured in DMEM supplemented with 10% FBS, streptomycin (100 $\mu$g $mL^{-1}$) and penicillin (100 U $mL^{-1}$) at 37 °C in a humidified 5% $CO_2$ atmosphere. C6 glioma cells were seeded in a 96-well plate at $1 \times 10^4$ per well under 100% humidity and cultured in DMEM medium for 24 h. The medium containing MnO-TETT and MnO-TETT-FA NPs were added in a dilution series (cell medium contained 0, 6.25, 12.5, 25, 50, and 100 $\mu M^{-1}$ Mn). After 24 h of incubation of cells with MnO-TETT and MnO-TETT-FA NPs, respectively, MTT solution (100 $\mu$L, 0.5 mg $mL^{-1}$) was added into each well. After incubation for another 4 h, the medium was discarded and DMSO was added into each well. The optical density (OD) value was measured on an enzyme-linked immunosorbent assay plate reader at a wavelength of 570 nm (Thermo Electron Corporation, USA). The cell viability was assessed and data were presented as the mean value with standard deviations from three independent experiments.

**Tiny Brain Glioma Model.** All animal experiments were performed according to protocols evaluated and approved by the ethical committee of Capital Medical University (Beijing, China). Male nude mice (BALB/C, 18−20 g, $n$ = 6) were anesthetized with 6% Chloral Hydrate (i.p., 0.15 mL/20 g) and placed in a stereotactic frame. A burrhole was drilled into the skull (1.0 mm anterior and 2.0 mm lateral to the bregma). C6 cells ($5 \times 10^5$) in 5 $\mu$L of DMEM were injected into the left brain with a 5 $\mu$L microinjector (Hamilton, Reno, NV). The injection was done slowly over 5 min, and the needle was kept in for 10 min and withdrawn after another 10 min. The burrhole was filled with bone wax and the skin was closed with nonmagnetic structures. MRI on nude mice bearing tumors was performed when the tumors reached 1.5−1.8 mm in diameter.

**MR Imaging of Tiny Gliomas.** The tiny brain glioma bearing mice were anesthetized with 6% chloral hydrate (i.p., 0.15 mL/20g). In vivo $T_1$-weighted MR images were acquired before and after the injection of MnO-TETT or MnO-TETT-FA NPs (8 mg Mn/kg body) into tail vein with a wrist coil on a 7.0 T MRI scanner (Bruker Pharmascan, Germany). The measurement parameters were as follows, TR = 250 ms, TE = 10 ms, FA = 141.6°, matrix = 256 × 256, FOV = 2.5 cm × 2.5 cm, number of experiment (NEX) = 10, slice thickness = 1 mm. The signal intensity of tumor was obtained at the region of interest (ROI) with the same diameter placed at the tumor site in the same slice on $T_1$-weighted images before or after the administration of MnO-TETT or MnO-TETT-FA NPs.

**Histology.** The ICR mice were sacrificed four weeks after injection of MnO NPs at a dosage of 26 mg Mn $kg^{-1}$. The major organs (heart, liver, kidney, spleen, lung, and brain) were soaked into 4% paraform for at least 24 h. Then, the tissues were then embedded in paraffin, sectioned into 5 $\mu$m slices, and stained with hematoxylin and eosin (HE) according to standard clinical pathology protocols. The stained sections were examined under a microscope (Nikon Eclipse E600, Nikon Inc., Melville, NY) at 100× magnification.

**Biodistrixbution.** The tumor-bearing mice ($n$ = 3 for each group) were injected intravenously with MnO-TETT or MnO-TETT-FA NPs. The mice were sacrificed at 24 h post injection. The brain, heart, liver, spleen, kidneys, and lungs were harvested, weighted, dissolved in the mixture of 30% hydrogen peroxide solution and nitric acid, and digested using a microwave digest system (CEM, Mars 5, USA). The content of Mn in different organs was then determined by ICP-OES.

## 3. RESULTS AND DISCUSSION

**Synthesis and Characterization of MnO-TETT-FA NPs.** The MnO-OA NPs were synthesized by thermal decomposition of manganese oleate in 1-octadecene. TEM images revealed that MnO-OA NPs were well separated (Figure 1A) and had a mean diameter of 16.8 ± 1.87 nm by measuring and averaging 100 of MnO-OA NPs. The HRTEM image of an

individual MnO-OA NP showed clear lattice fringes (Figure 1C), proving the crystalline nature of MnO NPs. The *d*-spacing value between lattice fringes was measured to be 0.27 nm, corresponding to the (111) plane of cubic phase MnO. The highly crystalline nature of MnO-OA NPs was further confirmed by the corresponding selected area electron diffraction (SAED) pattern (inset, Figure 1C). The average size of MnO-OA NPs measured by dynamic light scattering (DLS) was about 18 nm (Figure 1B), which is in agreement with the TEM result. Moreover, Figure 1D provides the field-dependent magnetization curve measured at room temperature. No remanence coercivity at zero field was observed, indicating the paramagnetic property of MnO NPs.[32]

The crystalline structure of MnO-OA NPs was further probed by powder XRD. All reflections shown in Figure 2 can be indexed to a cubic rock salt structure of MnO with characteristic peaks of (111), (200), (220), (311), and (222) by referring Joint Committee for Powder Diffraction Standards (JCPDS) card no. 75-0257. No traces of other manganese oxide phases were detected. The broadening of the diffraction peaks verified the nanocrystalline nature of MnO. Accordingly, the size of MnO-OA NPs was calculated to be about 16 nm using the Debye−Scherrer equation, which is consistent with the results of TEM image and DLS measurement.

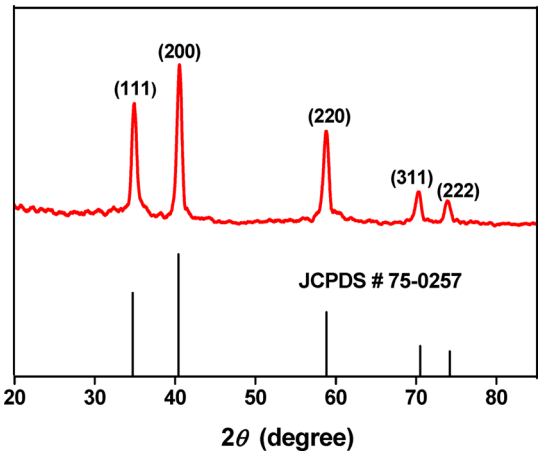


**Figure 2.** XRD pattern of MnO-OA NPs and JCPDS card No. 75-0257.

Highly water-dispersible MnO-TETT NPs were then obtained by exchanging OA ligands with TETT silane. Subsequently, the glioma-specific MnO-TETT-FA NPs were fabricated by conjugation of FA-PEG onto MnO-TETT NPs using the well-known EDC/NHS reaction. The TEM images of MnO-TETT (Figure 3A) and MnO-TETT-FA NPs (Figure 3C) indicated that there were no notable changes in the size. However, the edge of NPs became blurred, possibly due to the corrosion of MnO by the carboxylic silane. The average hydrodynamic diameters of MnO-TETT and MnO-TETT-FA NPs were approximately 142 (Figure 3B) and 122 nm (Figure 3D), respectively. The increase in hydrodynamic diameter, which is the common phenomenon when hydrophobic NPs were transformed into hydrophilic ones, is an indicative of aggregation. Nonetheless, both MnO NPs could be well dispersed in PBS and remained stable even at concentration of 15 mg $mL^{-1}$ for weeks (insets), suggesting the excellent water dispersibility and colloidal stability, which was attributed to the presence of repulsive forces between the large amount of carboxyl group on the surface of MnO NPs limiting the further aggregation.

FTIR spectra of MnO-OA, MnO-TETT, and MnO-TETT-FA NPs were obtained to verify the exchange of OA by TETT silane and the subsequent conjugation of FA-PEG (Figure 4A). In the IR spectrum of MnO-OA, a pair of bands at 2922 and

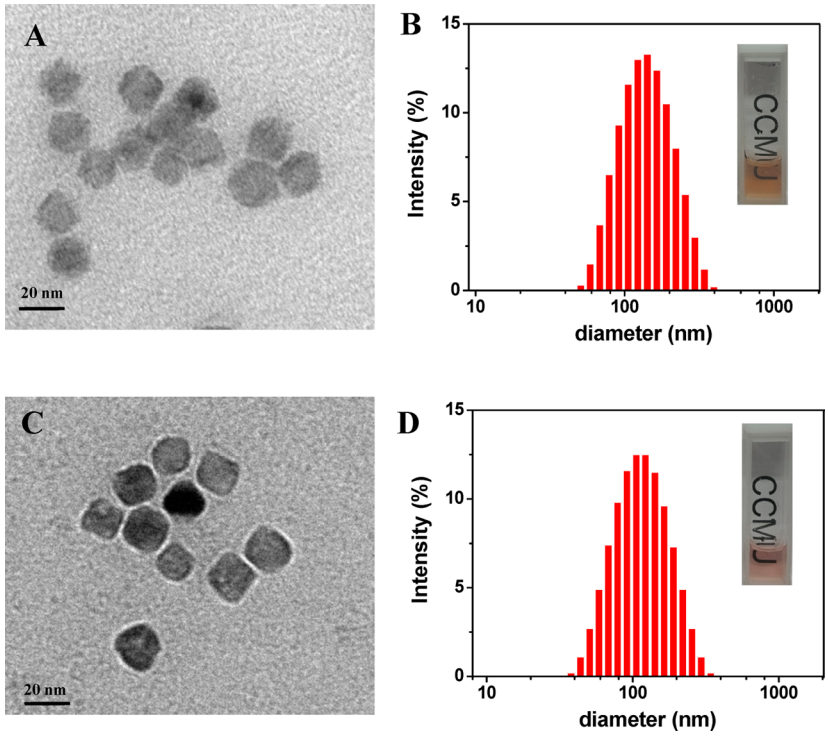


**Figure 3.** TEM images of (A) MnO-TETT and (C) MnO-TETT-FA NPs and size distribution of (B) MnO-TETT and (D) MnO-TETT-FA NPs. (inset) Digital pictures of MnO-TETT and MnO-TETT-FA NPs dispersed in PBS (15 mg $mL^{-1}$).

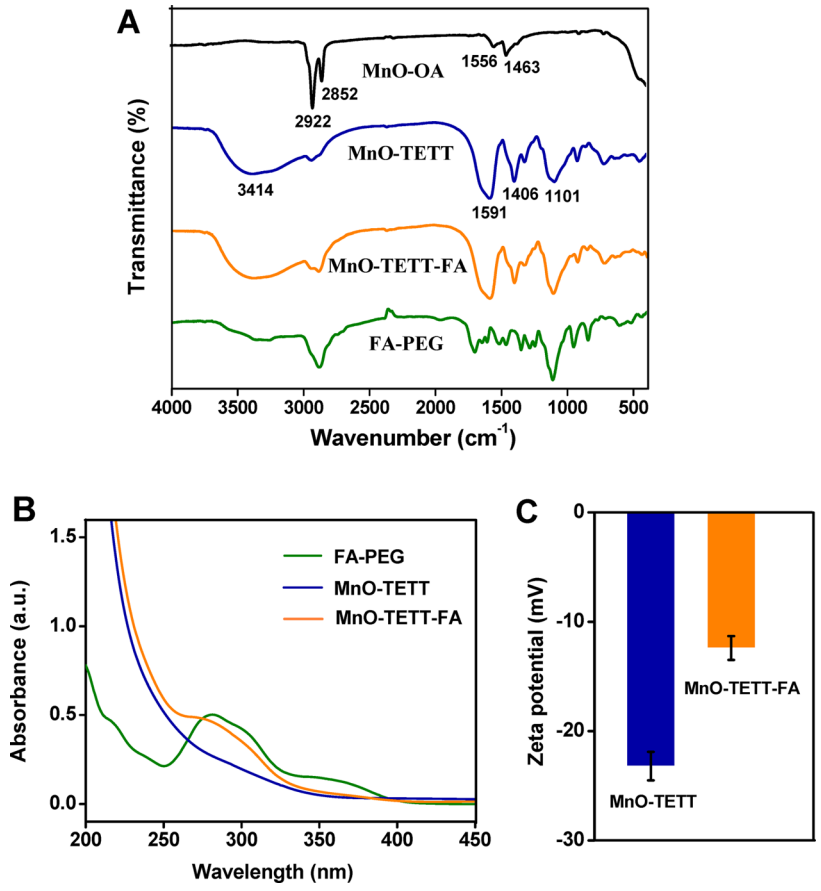


**Figure 4.** (A) IR spectra of MnO-OA, MnO-TETT, and MnO-TETT-FA NPs and FA-PEG, (B) UV−vis absorption spectra of FA-PEG, MnO-TETT, and MnO-TETT-FA, and (C) Zeta potential of MnO-TETT and MnO-TETT-FA NPs. Each result represents the mean ± SD of three runs.

2852 $cm^{-1}$ and another pair of bands at 1556 and 1463 $cm^{-1}$ were attributed to the characteristic $-CH_2-$ and $COO^-$ stretching of OA, respectively. These bands, however, almost disappeared in the IR spectrum of MnO-TETT. This together with the appearance of new characteristic bands of TETT such as Si−C and C−N band at 1328−1101 $cm^{-1}$ and intensive $COO^-$ band at 1591 and 1406 $cm^{-1}$ thus verified the replacement of OA by TETT silane. Additionally, the broad O−H stretching mode centered at 3414 $cm^{-1}$ suggested the hydrophilic nature of MnO-TETT NPs. The conjugation of FA-PEG onto MnO-TETT NPs was evidenced by the obvious increase in intensity of bands at 2922, 2852, and 1110 $cm^{-1}$ assigned to $CH_2$ and C−O−C of PEG and the broadening of band at 1591 $cm^{-1}$ due to the stretching vibrations of the aromatic ring of FA molecules. The attachment of FA-PEG was further verified by the appearance of characteristic shoulder of FA (around $\lambda$ = 363 nm) in the UV−vis absorption spectrum of MnO-TETT-FA (Figure 4B) and the change of zeta potential from −23.2 ± 1.3 to −12.4 ± 1.1 mV (Figure 4C).

**Relaxivity.** The efficiency of $T_1$ contrast agents is quantified by the longitudinal ($r_1$) relaxivity, where a higher value of $r_1$ corresponds to a greater MRI contrast effect.[34] As plotted in Figure 5A, the relaxivity value of MnO-TETT NPs was determined to be 4.84 $mM^{-1}$ $s^{-1}$, which is greater than that of most MnO NPs reported in the literature.[9−13] Relaxivity refers to the change in the relaxation rates of the water protons in the presence of contrast agents and only protons in close proximity to ion is relaxed. Therefore, a direct contact between surface Mn ion and water is required. Furthermore, the shorter the distance between surface Mn ion and proton is, the higher relaxivity is. In our case, the molecular thickness of TETT silane layer ensures a short distance between external Mn ion and water proton and thus leads to a high longitudinal relaxivity. The $r_1$ value of MnO-TETT-FA was 4.83 $mM^{-1}$ $s^{-1}$ (Figure 5B), suggesting that conjugation of FA-PEG onto MnO-TETT led to no adverse effect on the $r_1$ value. Accordingly, the corresponding $R_1$ maps exhibited a continuous increase in brightness, further demonstrating the potential of MnO-TETT and MnO-TETT-FA NPs as an efficient $T_1$ contrast agent.

**In Vitro and in Vivo Toxicity.** Prior to in vivo MRI study, the cytotoxicity of MnO-TETT and MnO-TETT-FA NPs toward 3T3 and C6 glioma cells was evaluated by the MTT assay. Figure 6 illustrates the 3T3 and C6 cell viabilities after incubation with MnO-TETT or MnO-TETT-FA NPs for 24 h at equivalent Mn concentrations of 6.25, 12.5, 25.0, 50.0, and 100 $\mu$M. No significant loss in cell viability at all tested concentrations, indicating the low cytotoxicity of MnO-TETT and MnO-TETT-FA NPs.

Furthermore, histological analysis was performed to assess the in vivo toxicity of MnO-TETT and MnO-TETT-FA NPs. Major organs (brain, heart, liver, spleen, lung, and kidney) of ICR mice were harvested 4 weeks after injection of MnO-TETT or MnO-TETT-FA NPs at a dosage of 26 mg Mn $kg^{-1}$ body, which was about three times higher than that administered for the following MRI scanning. As shown in Figure 7, no notable toxicity was observed in the tissues from the animals receiving MnO-TETT or MnO-TETT-FA NPs in

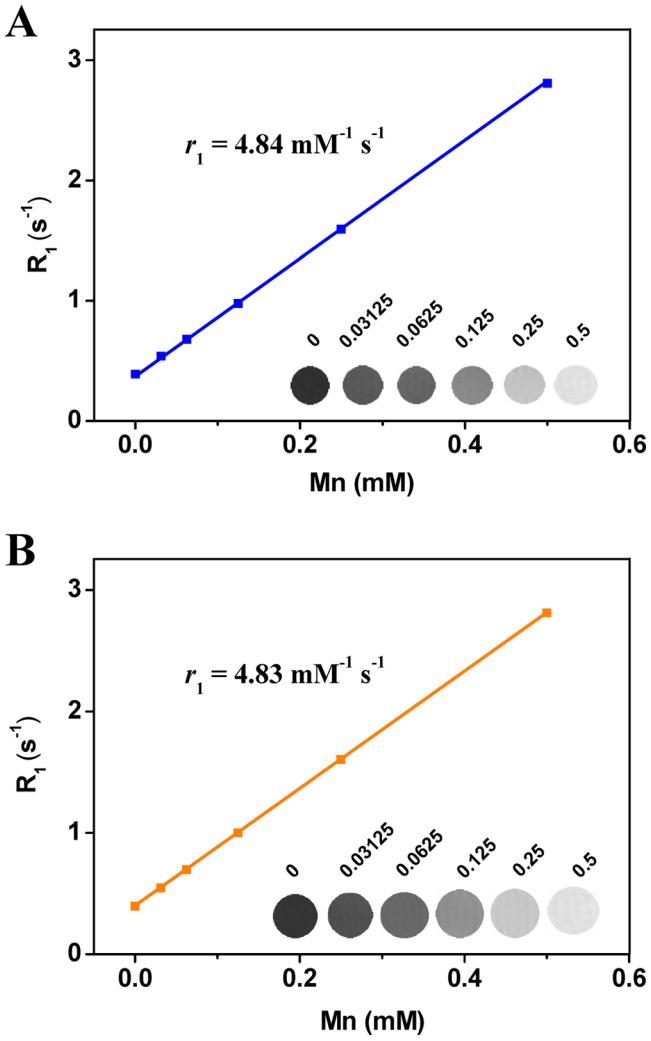


**Figure 5.** $r_1$ relaxivities of (A) MnO-TETT and (B) MnO-TETT-FA NPs.

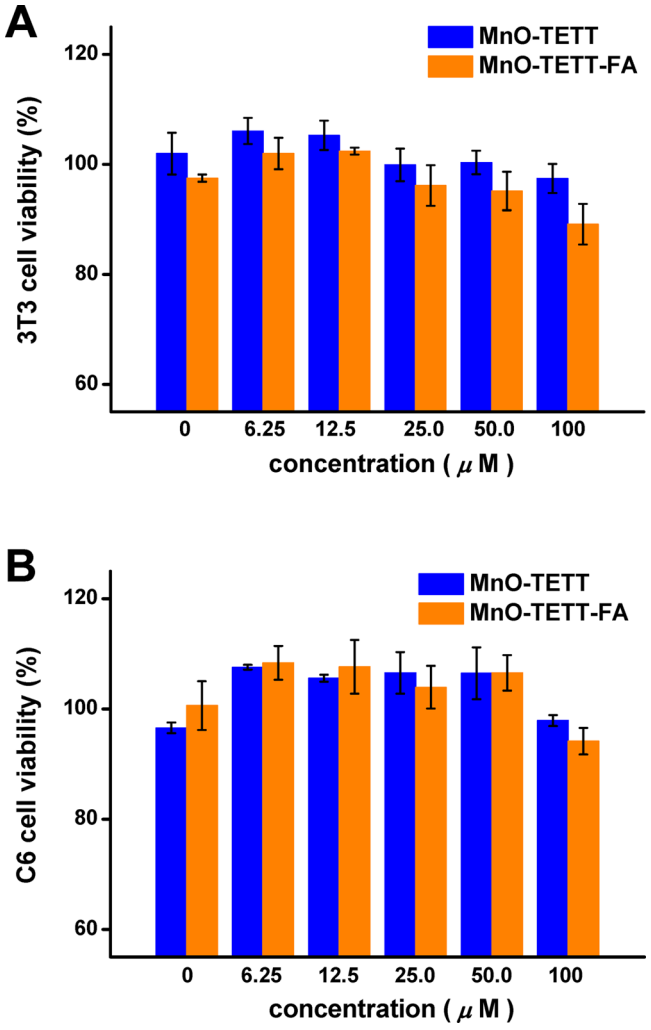


**Figure 6.** Viability of 3T3 (A) and C6 glioma (B) cells after 24 h incubation with MnO-TETT or MnO-TETT-FA NPs at various equivalent Mn concentrations. Each data represents the mean ± SD of three independent experiments.

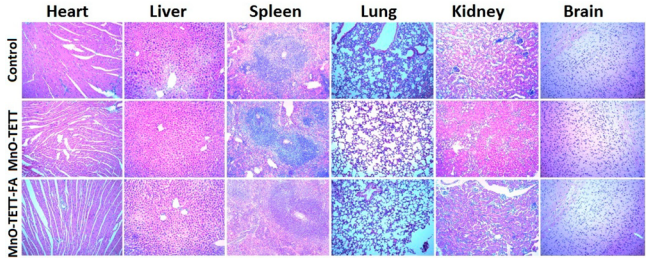


**Figure 7.** HE-stained tissue sections from mice receiving no injection and 4 weeks postinjection of MnO-TETT and MnO-TETT-FA NPs. Tissues were harvested from heart, liver, spleen, lung, kidney, and brain.

comparison with the control group (receiving no injection). For instance, no different inflammatory cells, thrombosis, and structural changes occurred in the brain. Meanwhile, no different dissolution, atrophy, and necroses of cardiac cells were observed in the heart, and no different degeneration and necrosis were detected in both hepatic cells and epithelia cells of renal tubule of the rats. The histological assessment thus indicated that both MnO NPs were biocompatible. However, long-term study is still needed to further evaluate the in vivo toxicity of these MnO NPs.

**MR Imaging of Tiny Brain Gliomas.** In order to evaluate the targeting ability of MnO-TETT-FA NPs, the tiny C6 brain glioma-bearing mouse model was established by inoculating 5 × $10^5$ C6 cells at the left brain. When the tumor reached 1.5–1.8 mm in diameter (about 14 day after implantation), the dynamic MR $T_1$-weighted images of transverse sections of gliomas were recorded pre/postinjection of MnO-TETT or MnO-TETT-FA NPs at a dosage of 8 mg Mn kg$^{-1}$ body. As shown in Figure 8, both MnO-TETT and MnO-TETT-FA NPs exhibited an obvious contrast enhancement in the tiny glioma 10 min, 2 h, and 24 h postinjection compared to the preinjection image. Nevertheless, the tumor margin was unclear over the scanning period for the MnO-TETT group. This is probably due to the fact that accumulation of MnO-TETT NPs in the tumor is dominated by the EPR effect. However, the EPR effect along is unable to make NPs adhere to or enter the cancer cells, which inevitably results in a blurred margin due to the diffusion of NPs. In contrast, the margin between glioma and normal tissue was clearly delineated for tiny glioma-bearing mice treated with MnO-TETT-FA NPs due to the specific and selective binding of FA to its receptor on the surface of glioma cells, which simultaneously increases the accumulation and


dx.doi.org/10.1021/am505223t | ACS Appl. Mater. Interfaces 2014, 6, 19850–19857

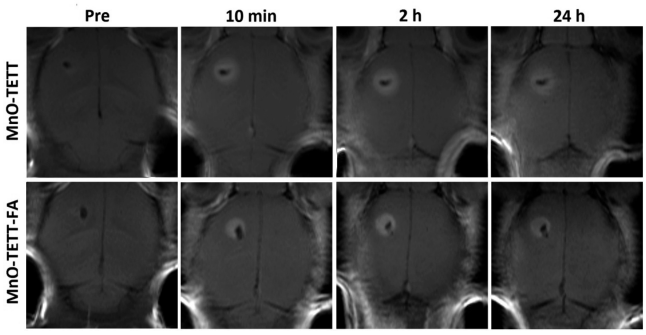


**Figure 8.** MR images of mice brain bearing tiny glioma pre- and 10 min, 2 h, and 24 h postintravenous injection of MnO-TETT NPs (upper panel) or MnO-TETT-FA NPs (lower panel).

minimizes the occurrence of diffusion. Apparently, the greater contrast enhancement and the clearer tumor margin signify the potential of MnO-TETT-FA as an effective MRI contrast agent for tiny brain glioma. Moreover, the enhanced contrast could be maintained up to 24 h, which offers additional benefits for intraoperative visualization of gliomas or monitoring of treatment response.

To further verify and differential the contrast enhancement induced by MnO-TETT-FA and MnO-TETT NPs in tumor areas, MRI signal intensity (SI) of the tumor tissue was quantified by setting the SI of the preinjection as 100%.[35] As expected, increases in SI postinjection were observed for either MnO-TETT or MnO-TETT-FA NPs (Figure. 9), suggesting

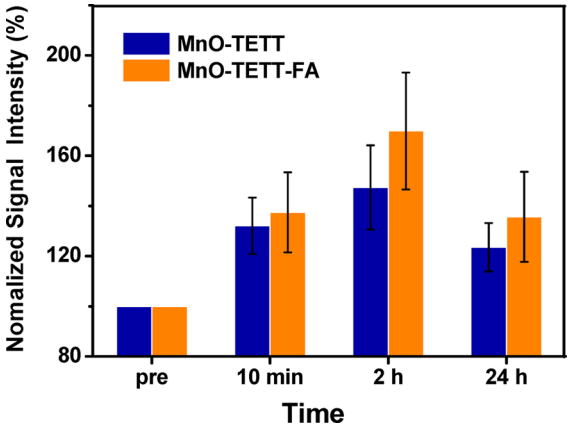


**Figure 9.** Quantification of the signal intensity enhancement in glioma-bearing mice according to MR images obtained before and 10 min, 2 h, and 24 h postinjection of MnO-TETT or MnO-TETT-FA NPs at a dosage of 8 mg Mn $kg^{-1}$ body.

that MnO NPs were prone to enter and accumulate in glioma region. Most importantly, the MnO-TETT-FA NPs exhibited even higher SI change than that of MnO-TETT at all scanning time points, especially at 2 and 24 h postinjection, demonstrating that high binding affinity of FA for brain glioma that helps enhance the contrast of the tumor region.

**Biodistribution.** Additionally, the biodistribution of MnO-TETT-FA and MnO-TETT NPs in glioma-bearing mice, which is of great importance for their further in vivo biomedical imaging applications, was evaluated by measuring the content of Mn in major organs. As shown in Figure 10, both MnO-TETT-FA and MnO-TETT NPs exhibited a higher distribution in the kidney than that in other organs, suggesting that MnO

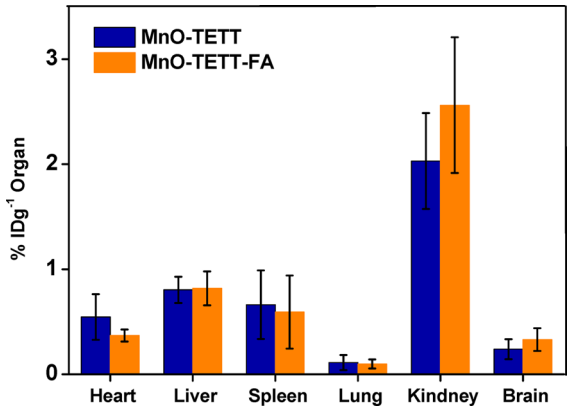


**Figure 10.** Biodistribution of MnO-TETT and MnO-TETT-FA NPs in tiny brain glioma bearing mice.

NPs were mainly excreted via the renal clearance route. In contrast, the lower Mn content in the lung indicated no undesirable accumulation. Although the content of Mn was relatively lower in brain than most other organs (except lung), the accumulation of MnO-TETT-FA NPs in the tiny-glioma bearing brain was indeed greater than that of MnO-TETT NPs. This thus additionally illustrates the role of FA in effective delivery of the contrast agent to the gliomas in vivo, leading to an enhance accumulation and consequently a successful MRI of tiny gliomas.

## 4. CONCLUSION

In summary, MnO-TETT-FA NPs with improved longitudinal relaxivity as potential glioma-targeted $T_1$ contrast agents were synthesized and characterized. The in vivo MR imaging demonstrated that MnO-TETT-FA NPs exhibited an enhanced contrast effect in the tiny glioma region with a prolonged imaging period. Moreover, MnO-TETT-FA NPs led to a clearer margin of the tiny glioma. This together with the good biocompatibility makes MnO-TETT-FA NPs a promising $T_1$ contrast agent for better detection and delineation of brain gliomas at the early stage.

## AUTHOR INFORMATION

### Corresponding Authors

*E-mail: weigu@ccmu.edu.cn (W.G.).
*E-mail: lingye@ccmu.edu.cn (L.Y.).
*E-mail: cjyu1955@sina.com (C.Y.).

### Notes

The authors declare no competing financial interest.

## ACKNOWLEDGMENTS

The authors gratefully acknowledge the financial support from the Natural Science Foundation of China (81271639, 81372694), the Beijing Municipal Foundation for the Talents (2011D005018000001), the Basic-clinical Key Research Grant (13JL02) from Capital Medical University, the Open Project Program of Key Laboratory for Neurodegenerative Diseases of the Ministry of Education (2012NZDJ01), and Beijing Sanbo Brain Hospital Advance research program of innovation (2012SJ005).

## REFERENCES


(1) Wang, J.; Huang, Y.; David, A. E.; Chertok, B.; Zhang, L.; Yu, F.; Yang, V. C. Magnetic Nanoparticles for MRI of Brain Tumors. *Curr. Pharm. Biotechnol.* **2012**, *13*, 2403−2416.

(2) Weissleder, R.; Pittet, M. J. Imaging in the Era of Molecular Oncology. *Nature* **2008**, *452*, 580−589.

(3) Cao, Y.; Sundgren, P. C.; Tsien, C. I.; Chenevert, T. T.; Junck, L. Physiologic and Metabolic Magnetic Resonance Imaging in Gliomas. *J. Clin. Oncol.* **2006**, *24*, 1228−1235.

(4) Pishko, G. L.; Astary, G. W.; Mareci, T. H.; Sarntinoranont, M. Sensitivity Analysis of an Image-based Solid Tumor Computational Model with Heterogeneous Vasculature and Porosity. *Ann. Biomed. Eng.* **2011**, *39*, 2360−2373.

(5) Geninatti Crich, S.; Cabella, C.; Barge, A.; Belfiore, S.; Ghirelli, C.; Lattuada, L.; Lanzardo, S.; Mortillaro, A.; Tei, L.; Visigalli, M.; Forni, G.; Aime, S. *In Vitro* and *In Vivo* Magnetic Resonance Detection of Tumor Cells by Targeting Glutamine Transporters with Gd-based Probes. *J. Med. Chem.* **2006**, *49*, 4926−4936.

(6) Luo, K.; Liu, G.; Zhang, X.; She, W.; He, B.; Nie, Y.; Li, L.; Wu, Y.; Zhang, Z.; Gong, Q. Functional L-Lysine Dendritic Macromolecules as Liver-Imaging Probes. *Macromol. Biosci.* **2009**, *9*, 1227−1236.

(7) Zhou, Z.; Lu, Z. R. Gadolinium-based Contrast Agents for Magnetic Resonance Cancer Imaging. *Wiley Interdiscip. Rev. Nanomed. Nanobiotechnol.* **2013**, *5*, 1−18.

(8) Pan, D.; Schmieder, A. H.; Wickline, S. A.; Lanza, G. M. Manganese-based MRI Contrast Agents: Past, Present, and Future. *Tetrahedron* **2011**, *67*, 8431−8444.

(9) Shin, J.; Anisur, R. M.; Ko, M. K.; Im, G. H.; Lee, J. H.; Lee, I. S. Hollow Manganese Oxide Nanoparticles as Multifunctional Agents for Magnetic Resonance Imaging and Drug Delivery. *Angew. Chem., Int. Ed.* **2009**, *48*, 321−324.

(10) Huang, J.; Xie, J.; Chen, K.; Bu, L.; Lee, S.; Cheng, Z.; Li, X.; Chen, X. HSA Coated MnO Nanoparticles with Prominent MRI Contrast for Tumor Imaging. *Chem. Commun.* **2010**, *46*, 6684−6686.

(11) Huang, C. C.; Khu, N. H.; Yeh, C. S. The Characteristics of Sub 10 nm Manganese Oxide $T_1$ Contrast Agents of Different Nanostructured Morphologies. *Biomaterials* **2010**, *31*, 4073−4078.

(12) Yang, H.; Zhuang, Y.; Hu, H.; Du, X.; Zhang, C.; Shi, X.; Wu, H.; Yang, S. Silica-Coated Manganese Oxide Nanoparticles as a Platform for Targeted Magnetic Resonance and Fluorescence Imaging of Cancer Cells. *Adv. Funct. Mater.* **2010**, *20*, 1733−1741.

(13) Schladt, T. D.; Shukoor, M. I.; Schneider, K.; Tahir, M. N.; Natalio, F.; Ament, I.; Becker, J.; Jochum, F. D.; Weber, S.; Kohler, O.; Theato, P.; Schreiber, L. M.; Sonnichsen, C.; Schroder, H. C.; Muller, W. E.; Tremel, W. Au@MnO Nanoflowers: Hybrid Nanocomposites for Selective Dual Functionalization and Imaging. *Angew. Chem., Int. Ed.* **2010**, *49*, 3976−3980.

(14) Kim, T.; Momin, E.; Choi, J.; Yuan, K.; Zaidi, H.; Kim, J.; Park, M.; Lee, N.; McMahon, M. T.; Quinones-Hinojosa, A.; Bulte, J. W. M.; Hyeon, T.; Gilad, A. A. Mesoporous Silica-Coated Hollow Manganese Oxide Nanoparticles as Positive $T_1$ Contrast Agents for Labeling and MRI Tracking of Adipose-Derived Mesenchyrnal Stem Cells. *J. Am. Chem. Soc.* **2011**, *133*, 2955−2961.

(15) Faucher, L.; Tremblay, M.; Lagueux, J.; Gossuin, Y.; Fortin, M.-A. Rapid Synthesis of PEGylated Ultrasmall Gadolinium Oxide Nanoparticles for Cell Labeling and Tracking with MRI. *ACS Appl. Mater. Interfaces* **2012**, *4*, 4506−4515.

(16) Peer, D.; Karp, J. M.; Hong, S.; Farokhzad, O. C.; Margalit, R.; Langer, R. Nanocarriers as an Emerging Platform for Cancer Therapy. *Nat. Nanotechnol.* **2007**, *2*, 751−760.

(17) Im, G. H.; Kim, S. M.; Lee, D. G.; Lee, W. J.; Lee, J. H.; IS, L. $Fe_3O_4$/MnO Hybrid Nanocrystals as a Dual Contrast Agent for Both $T_1$- and $T_2$-weighted Liver MRI. *Biomaterials* **2013**, *34*, 2069−2076.

(18) Wankhede, M.; Bouras, A.; Kaluzova, M.; Hadjipanayis, C. G. Magnetic Nanoparticles: an Emerging Technology for Malignant Brain Tumor Imaging and Therapy. *Expert Rev. Clin. Pharmacol.* **2012**, *5*, 173−186.

(19) Aina, O. H.; Sroka, T. C.; Chen, M. L.; Lam, K. S. Therapeutic Cancer Targeting Peptides. *Biopolymers* **2002**, *66*, 184−199.

(20) Tomanek, B.; Iqbal, U.; Blasiak, B.; Abulrob, A.; Albaghdadi, H.; Matyas, J. R.; Ponjevic, D.; Sutherland, G. R. Evaluation of Brain Tumor Vessels Specific Contrast Agents for Glioblastoma Imaging. *Neuro-oncology* **2012**, *14*, 53−63.

(21) Licciardi, M.; Scialabba, C.; Cavallaro, G.; Sangregorio, C.; Fantechi, E.; Giammona, G. Cell Uptake Enhancement of Folate Targeted Polymer Coated Magnetic Nanoparticles. *J. Biomed. Nanotechnol.* **2013**, *9*, 949−964.

(22) Kang, C.; Yuan, X.; Li, F.; Pu, P.; Yu, S.; Shen, C.; Zhang, Z.; Zhang, Y. Evaluation of Folate-PAMAM for the Delivery of Antisense Oligonucleotides to Rat C6 Glioma Cells *In Vitro* and *In Vivo*. *J. Biomed. Mater. Res., Part A* **2010**, *93*, 585−594.

(23) Weitman, S. D.; Frazier, K. M.; Kamen, B. A. The Folate Receptor in Central Nervous System Malignancies of Childhood. *J. Neurooncol.* **1994**, *21*, 107−112.

(24) Zhao, X.; Li, H.; Lee, R. J. Targeted drug delivery via folate receptors. *Expert Opin. Drug Delivery* **2008**, *5*, 309−319.

(25) Chauhan, R. P.; Mathur, R.; Singh, G.; Kaul, A.; Bag, N.; Singh, S.; Kumar, H.; Patra, M.; Mishra, A. K. Evaluation of Folate Conjugated Superparamagnetic Iron Oxide Nanoparticles for Scintigraphic/Magnetic Resonance Imaging. *J. Biomed. Nanotechnol.* **2013**, *9*, 323−334.

(26) Lu, Y.; Low, P. S. Folate-mediated Delivery of Macromolecular Anticancer Therapeutic Agents. *Adv. Drug Delivery Rev.* **2002**, *54*, 675−693.

(27) Bulte, J. W.; Kraitchman, D. L. Iron Oxide MR Contrast Agents for Molecular and Cellular Imaging. *NMR Biomed.* **2004**, *17*, 484−499.

(28) Na, H. B.; Lee, J. H.; An, K.; Park, Y. I.; Park, M.; Lee, I. S.; Nam, D. H.; Kim, S. T.; Kim, S. H.; Kim, S. W. Development of a $T_1$ Contrast Agent for Magnetic Resonance Imaging using MnO Nanoparticles. *Angew. Chem., Int. Ed.* **2007**, *119*, 5497−5401.

(29) Lee, J. H.; Huh, Y. M.; Jun, Y. W.; Seo, J. W.; Jang, J. T.; Song, H. T.; Kim, S.; Cho, E. J.; Yoon, H. G.; Suh, J. S.; Cheon, J. Artificially Engineered Magnetic Nanoparticles for Ultra-sensitive Molecular Imaging. *Nat. Med.* **2007**, *13*, 95−99.

(30) Qi, Y.; Shao, C.; Gu, W.; Li, F.; Deng, Y.; Li, H.; Ye, L. Carboxylic Silane-exchanged Manganese Ferrite Nanoclusters with High Relaxivity for Magnetic Resonance Imaging. *J. Mater. Chem. B* **2013**, *1*, 1846−1851.

(31) Xiao, J.; Tian, X. M.; Yang, C.; Liu, P.; Luo, N. Q.; Liang, Y.; Li, H. B.; Chen, D. H.; Wang, C. X.; Li, L.; Yang, G. W. Ultrahigh Relaxivity and Safe Probes of Manganese Oxide Nanoparticles for *In Vivo* Imaging. *Sci. Rep.* **2013**, *3*, 3424.

(32) Park, J.; Bang, D.; Kim, E.; Yang, J.; Lim, E.-K.; Choi, J.; Kang, B.; Suh, J.-S.; Park, H. S.; Huh, Y.-M.; Haam, S. Effect of Ligand Structure on MnO Nanoparticles for Enhanced $T_1$ Magnetic Resonance Imaging of Inflammatory Macrophages. *Eur. J. Inorg. Chem.* **2012**, 5960−5965.

(33) Li, X.; Shao, J.; Qin, Y.; Shao, C.; Zheng, T.; Ye, L. TAT-conjugated nanodiamond for the enhanced delivery of doxorubicin. *J. Mater. Chem.* **2011**, *21*, 7966−7973.

(34) Hao, R.; Xing, R.; Xu, Z.; Hou, Y.; Gao, S.; Sun, S. Synthesis, Functionalization, and Biomedical Applications of Multifunctional Magnetic Nanoparticles. *Adv. Mater.* **2010**, *22*, 2729−2742.

(35) Xie, H.; Zhu, Y.; Jiang, W.; Zhou, Q.; Yang, H.; Gu, N.; Zhang, Y.; Xu, H.; Xu, H.; Yang, X. Lactoferrin-conjugated Superparamagnetic Iron Oxide Nanoparticles as a Specific MRI Contrast Agent for Detection of Brain Glioma *In Vivo*. *Biomaterials* **2011**, *32*, 495−502.